







Elastically induced magnetization at ultrafast time scales in a chiral helimagnet

Hengzhou Liu ^{1,*}, M. Tuan Trinh ^{1,*}, Eleanor M. Clements,¹ Deepak Sapkota,² Ling Li,² Zachary Romestan ³, Soumya Bhat ³, Varun Mapara,¹ Arup Barua ¹, Samuel Langelund Carrera ¹, Manh-Huong Phan,¹ Dario Arena,¹ Hariharan Srikanth,¹ David Mandrus,² Aldo H. Romero,³ and Denis Karaiskaj^{1,†}

¹Department of Physics, University of South Florida, Tampa, Florida 33620, USA

²Department of Materials Science and Engineering, University of Tennessee, Knoxville, Tennessee 37996, USA

³Department of Physics and Astronomy, West Virginia University, Morgantown, West Virginia 26506, USA



(Received 6 February 2022; revised 9 June 2022; accepted 21 June 2022; published 1 July 2022)

Chiral helimagnetic materials have recently attracted much attention for spintronic applications due to their long-range helical magnetic order, topological spin textures, and potential for hosting skyrmions. Their robust spin texture would provide a new concept of ultrafast magnetic memory if it can be controlled by an ultrafast optical pulse. Using time-resolved magneto-optical Kerr spectroscopy, we show that magnetism in the single-crystalline chiral helimagnet $\text{Cr}_{1/3}\text{NbS}_2$ can be induced by an ultrafast optical pulse. At low temperatures and in the absence of magnetic fields, $\text{Cr}_{1/3}\text{NbS}_2$ exhibits a chiral helical magnetic phase with a long-range helical spin order, but it contains zero net magnetization. However, after the laser pulse excitation we observe magnetization forming over tens of picoseconds, far exceeding the duration of the laser pulse. We attribute this peculiar behavior to a laser-induced phase transition from the chiral helimagnetic phase, with zero net magnetization, to a chiral conical helimagnetic phase, with finite magnetization. *Ab initio* density functional calculations provide a detailed microscopic picture of the mechanism behind the observation. The resonant magnon-phonon coupling with specific phonons leads to an elastic deformation of the chiral helimagnetic phase. Finally, at finite magnetic fields, the net magnetization is excited by the laser pulse and precesses around the equilibrium position, leading to anomalous magnetization precession as a function of the external magnetic field at specific magnetic phases.

DOI: [10.1103/PhysRevB.106.035103](https://doi.org/10.1103/PhysRevB.106.035103)

I. INTRODUCTION

In magnetic systems lacking crystal inversion symmetry, the anisotropic exchange interaction induced by spin-orbit coupling leads to antisymmetric Dzyaloshinskii-Moriya interactions (DMIs) [1–3]. Competition between symmetric exchange and DMIs can lead to a screwlike arrangement of the magnetic moments that induces a number of interesting phenomena, including chiral helimagnetic spin texture [4], skyrmion lattices [5,6], and the topological Hall effect [5]. Helical magnetism has been observed in a number of materials, including FeGe [7], MnSi [8], MnP [9], Cu_2OSeO_3 [10], $\text{Cr}_{1/3}\text{NbS}_2$ [11], etc. Among these, $\text{Cr}_{1/3}\text{NbS}_2$ has attracted particular attention due to its unique properties, such as its layered structure, topological spin texture, one-dimensional solitonic quasiparticles, and uniaxial spin windings [12]. The crystal structure of $\text{Cr}_{1/3}\text{NbS}_2$ is formed by 2H-type hexagonal two-dimensional layers of transition metal chalcogenide NbS_2 , intercalated by Cr ions in the octahedral holes [13]. Without Cr ions, NbS_2 layers are coupled via van der Waals interaction and can be exfoliated into monolayers. However, with the intercalation of Cr atoms, the bonding is strengthened due to the charge transfer from the Cr atoms to the Nb atoms,

which results in substantial changes of the electronic and magnetic properties of the crystal.

The $\text{Cr}_{1/3}\text{NbS}_2$ crystal exhibits a complicated phase diagram with multiple exotic magnetic phases depending on the temperature and applied magnetic fields. The ground state is chiral helimagnetic and is formed from the ferromagnetic exchange interaction favoring parallel arrangement of Cr electron spins in the *ab* plane and antiferromagnetic interaction of electron spins between two Cr intercalating layers. These two competing interactions combined with the isotropic and anisotropic exchange interactions arrange the spins parallel in the *ab* plane and twist them into a helix along the *c*-axis with left-handed chirality [11]. The application of magnetic fields below the Curie temperature (T_c) leads to the formation of the chiral soliton lattice (CSL) [11,14]. Unlike magnetic skyrmions, which exist in a narrow range of temperatures and magnetic fields [5], the CSL is robust and very stable over a wide range of temperatures. This robust spin structure leads to interesting phenomena observed in $\text{Cr}_{1/3}\text{NbS}_2$, including the ordinary and anomalous Hall effects [15], magnetoresistance [16], collective excitation modes [17], and magnetic soliton confinement [18].

Although much research has been done on the magnetic and structural properties of $\text{Cr}_{1/3}\text{NbS}_2$ as well as their related devices [13], little is known about the ultrafast spin dynamics and ultrafast domain switching in this crystal. Using optical pulses to manipulate magnetization has recently attracted considerable attention due to their ultrafast time scale,

*These authors contributed equally to this work.

†Corresponding author: karaiskaj@usf.edu

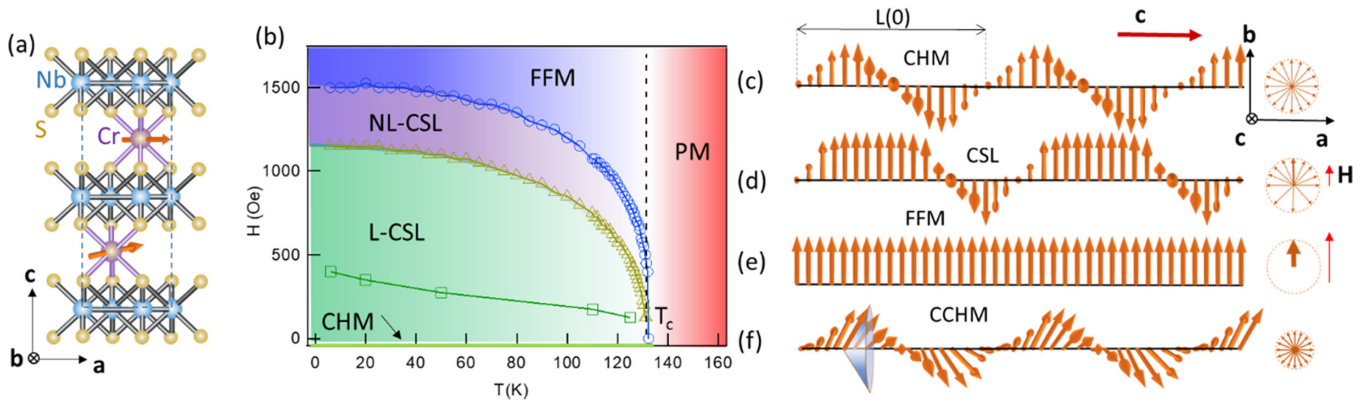


FIG. 1. Helical magnetic phases. (a) The $\text{Cr}_{1/3}\text{NbS}_2$ crystal structure with Cr atoms intercalated between 2H-NbS_2 layers. The dashed rectangle indicates the unit cell. (b) Phase diagram of $\text{Cr}_{1/3}\text{NbS}_2$ for magnetic fields perpendicular to the helical c -axis. Above $T_c = 132.3$ K, the crystal is in the paramagnetic phase (PM). (c) The chiral helimagnetic phase (CHM) in the absence of magnetic fields. (d) The chiral soliton lattice phase (CSL). In (b) triangles mark the boundary between the linear chiral soliton lattice (L-CSL) and the nonlinear soliton lattice (NL-CSL) (e) The forced ferromagnetic phase (FFM). In (b), above the circles the crystal is in the FFM phase, where all the spins are aligned along the direction of the external field. (f) Chiral conical helimagnetic phase (CCHM). On the right, the spin projections on the ab -plane are shown.

high efficiency, and applications such as sensing technology, quantum computing, terahertz technology, ultrafast optical switching, and ultrafast data storage [19]. In this article, we employ the ultrafast time-resolved magneto-optical Kerr effect (TR-MOKE) to investigate the ultrafast spin dynamics of the chiral helical magnet $\text{Cr}_{1/3}\text{NbS}_2$. We observe peculiar dynamics, where the magnetization generated by the laser increases far beyond the time duration of the optical pulse, with an even longer recovery. We theoretically describe this light-induced magnetism lasting three orders of magnitude beyond the temporal duration of the optical pulse as transforming the chiral helimagnetic phase to the chiral conical magnetic phase. Furthermore, we perform first-principles calculations within density functional theory (DFT) to understand the microscopic origin of this phenomenon. These calculations reveal precisely two phonon modes that intersect with the magnon spectrum and provide the elastic canting of the spins along the c -axis, leading to the chiral conical magnetic phase with a nonzero net magnetization. Finally, with increasing magnetic fields along the c -axis we map the dynamics across many different magnetic phases with strikingly different spin textures.

II. RESULTS

The known magnetic phases of the $\text{Cr}_{1/3}\text{NbS}_2$ crystal are shown in Fig. 1, starting with the ground state having zero net magnetization in the absence of external magnetic fields. Below the Curie temperature $T_c = 132$ K and at zero magnetic field, the crystal exhibits the chiral helimagnetic phase (CHM) with the winding period of ~ 48 nm [11], whereas at temperatures above T_c , the crystal is paramagnetic. The application of external magnetic fields along the c -axis leads to two chiral soliton lattice phases, depending on the strength of the magnetic field. At lower fields the linear chiral soliton lattice (L-CSL) is observed, whereas at higher fields the nonlinear chiral soliton lattice (NL-CSL) with a larger ferromagnetic array forms [20–22]. Further increase of the magnetic field aligns all spins in the direction of the magnetic field, trans-

forming CSL into the forced ferromagnetic (FFM) state. The phase boundaries shown in Fig. 1(b) were determined by measuring the magnetic entropy change and ac susceptibility as functions of magnetic field and temperature [21,23].

A. Laser-induced magnetization in the absence of external magnetic fields

Whereas the ultrafast demagnetization of a crystal with nonzero net magnetization in the ground state has been observed and studied in detail [24–27], the opposite effect, namely the generation of magnetization with a laser pulse, is rarely observed and is short-lived, typically in the subpicosecond range [28,29]. Thermal changes in magnetic anisotropy have been shown to lead to longer-lasting effects of several picoseconds [30]. Another method of generating ultrafast light-induced magnetism and magnetic domain switching in magnetic materials has been achieved using a circularly polarized laser pulse that acts as an effective magnetic field via the inverse Faraday effect [31–34]. Although linearly polarized laser pulses do not carry any angular momentum, they can generate magnetic fields through the inverse Cotton-Mouton effect [35], the nonlinear coupling of electric and magnetic fields of light [36,37], or via the impulsive stimulated Raman scattering using short laser pulses [38]. The latter crucially depends on the orientation of the linearly polarized light and the magnetic structure of the material, including the magneto-optical susceptibility and the spin-wave polarizability. In the absence of net magnetization in antiferromagnets, the inertia-driven spin switching mechanism was proposed to account for the observed magnetization oscillation, which assumes that the system is oscillating between two magnetization states at a time slower than the excitation pulse duration [39].

We start our discussion with the induced magnetization in the sample by a linearly polarized femtosecond laser pulse in the absence of any external magnetic fields. At zero magnetic fields, the ground state has zero net magnetization, and a Faraday rotation is induced solely by the linearly polarized pump laser pulse. The TR-MOKE signal at zero magnetic field is

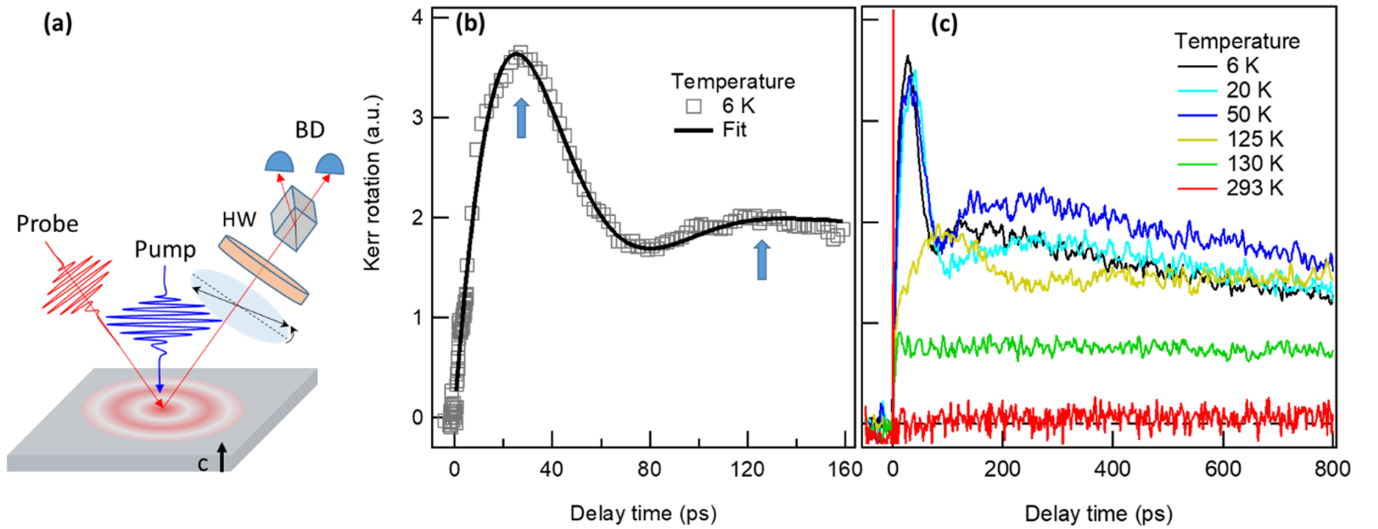


FIG. 2. Light-induced magnetism at zero field. (a) Schematic of the TR-MOKE measurement. (b) A short time scale of the TR-MOKE signal for $\text{Cr}_{1/3}\text{NbS}_2$ at 6 K. The solid curve is the fit using a damping sinusoidal function. The blue arrows mark two maxima in the Kerr rotation. (c) TR-MOKE signals for different temperatures at zero field.

shown in Fig. 2(b) as a function of the time delay between the pump and probe laser pulses. The pump pulse perturbs the spins, whereas the probe pulse tracks the spin dynamics as a function of time, shown schematically in Fig. 2(a). The signal tracks variations in the polarization of the reflected probe pulse caused by the changing magnetization of the crystal. At the lowest temperature in Fig. 2(b) we observe an increase of the TR-MOKE signals that lasts up to ~ 30 ps, much larger than the duration of the laser pulse of ~ 100 fs. The time evolution of the Kerr rotation resembles a damped oscillation between two phases with a second increase that peaks at around ~ 120 ps. The increase in Kerr rotation persists more than three orders of magnitude beyond the laser pulse duration, in the absence of external magnetic fields.

We interpret this observation as a slow transition between two phases: the zero net magnetization CHM phase and a new nonzero net magnetization phase, namely the chiral conical helimagnetic phase (CCHM) shown in Fig. 1(f). In Fig. 2(b) we fit the dynamics of this phase transition by a decaying sinusoidal function. The observed dynamics remains largely unchanged for temperatures well below $T_c = 132$ K, but becomes even slower and weaker for $T = 125$ K, as the temperature approaches T_c . The stability of the magnetization dynamics with temperature below T_c leads to the conclusion that thermal changes of the magnetic anisotropy are unlikely to cause the observed behavior [30]. Furthermore, the time scale spanning over tens of picoseconds to over 120 ps, much longer than the duration of the pump pulse, makes optical effects such as light-induced birefringence, changes in the magneto-optical constant, or generation of magnetic fields through the Cotton-Mouton effect unlikely [27–29]. The residual rotation Kerr signal decays on a much longer time scale of ~ 2 ns, obtained by a single exponential fit. It should be noted that at zero magnetic fields, the crystal is in CHM phase, which has a long-range spin order but contains no net magnetic moment. Therefore, the spin polarization in the present measurement is thought to be induced by the laser excitation. Laser heating cannot lead to a nonzero net mag-

netization phase as observed in FeRh [40–46], since the only possible outcome at higher temperature in the phase diagram is the paramagnetic phase.

To reveal the underlying mechanism behind the observed behavior, we perform first-principles calculations within DFT (see the Supplemental Material for details [47]). We build a spin model for $\text{Cr}_{1/3}\text{NbS}_2$ and consider the dynamic impact of the spin-lattice coupling on the orientation of the magnetic moments. Our calculations provide a detailed picture of the magnetic interactions in the $\text{Cr}_{1/3}\text{NbS}_2$ crystal. The exchange interaction between Cr ions in neighboring layers along the c -axis is strongly ferromagnetic, whereas the interaction between Cr species that separated by two layers along the c -axis is antiferromagnetic, with approximately only half the magnitude of the ferromagnetic interactions. Considering the Cr-Cr interactions alone, the competing antiferromagnetic interaction suggests a tendency for antiferromagnetic order across the unit cell, in which the spin direction alternates between each layer. Nonetheless, in addition to the Cr-Cr exchange interaction, there is considerable ferromagnetic exchange between the Cr and Nb ions. This ferromagnetic interaction counters the competing antiferromagnetic exchange, resulting in the expected short-range ferromagnetic order.

However, the isotropic exchange in our model reproduces the short-range behavior but provides no insights into the long-range helical order. The calculated anisotropic interactions reveal a symmetric anisotropic exchange oriented along the ab -plane with a similar magnitude to the isotropic exchange. Furthermore, there is a small uniaxial DMI component oriented along the negative c -axis. The strong anisotropic exchange causes the spin moments to favor in-plane alignment, whereas the uniaxial DMI component leads to the left-handed rotation along the c -axis. The combined effect of these interactions results in the chiral helimagnetic ground state in our model.

After capturing the static spin interactions using our theoretical calculations, we proceed with the dynamic magnetic

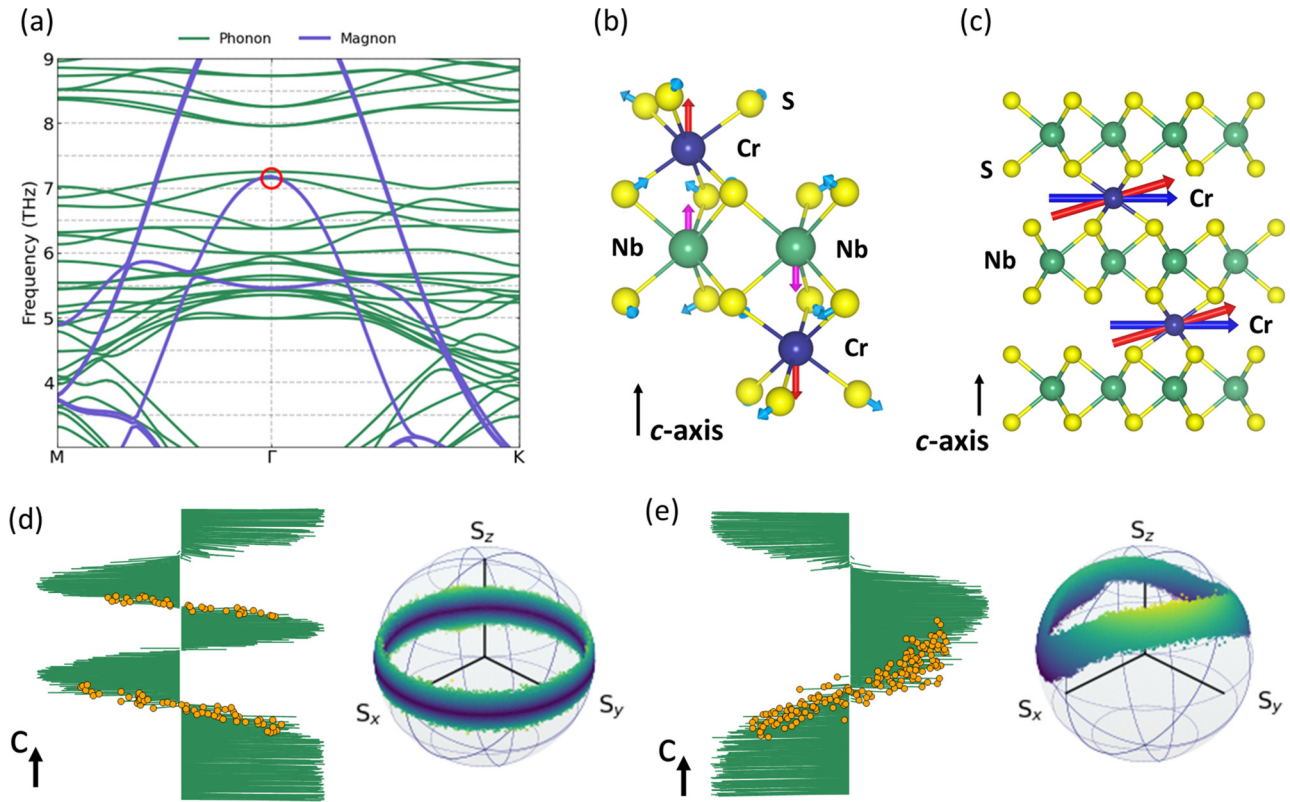


FIG. 3. Calculated phonon-magnon coupling. (a) The magnon spectrum for the isotropic and anisotropic Cr-Cr interactions is overlaid against the phonon spectra. The circle marker highlights the crossing that drives the emergent conical phase, corresponding to the frequency 7.15 THz at the zone center. (b) Displacement of the coherent phonon mode at the zone center. The arrows depict the direction of each individual atom. This mode is primarily characterized by the displacement of the Cr and Nb atoms along the c -axis. (c) Schematic of the Cr spins, where the blue arrow represents the unperturbed spin on the ab -plane, and the red arrow shows the canted spin along the c -axis. (d) The equilibrium spin configuration for $\text{Cr}_{1/3}\text{NbS}_2$ in the absence of the ~ 7.15 THz phonon. (e) The equilibrium spin configuration after introducing the normal mode displacements along the c -axis at ~ 7.15 THz. The projection of the spin orientations averaged over 4.5 ps onto a unit sphere is shown in (d) for the structure without displacements, and in (e) including the displacement by the 7.15 THz phonon. Comparing the spin configurations between the two cases reveals a propensity for the resonant phonon to reverse the chirality of the spin spiral, lengthen the spiral, and drive an emergent magnetic moment along the c -axis. In each plot, the lengths of the spinors are normalized to 1. The color gradient in (e) and (d) qualitatively represents the angle above or below the S_x - S_y plane.

properties and calculate the full magnon spectra. We further calculate the full phonon spectra and examine the dynamic spin-lattice coupling by comparing the magnon and phonon dispersions, shown in Fig. 3(a). The strongest spin-lattice coupling would occur when the fluctuations are coherent, which happens when the magnon and phonon bands intersect. By overlapping and carefully examining the magnon and phonon dispersions, two intersections near the zone center stand out. First, the low-lying magnon band related to the isotropic exchange crosses with an acoustic phonon mode and a low-frequency optical phonon mode. This intersecting phonon mode involves the rigid displacement of the Nb-S layers in the ab -plane. The normal mode displacement reduces the DMI component along the c -axis and increases the ab -plane components of the DMI of the interlayer Cr-Cr interactions. Thus, it leads to broadening and softening of the magnon bands associated with the anisotropic interactions near Γ , which reduces the energy barrier needed for magnetic excitation.

Furthermore, a second intersection occurs at the magnon band related to the anisotropic exchange, which overlaps with

the optical phonon branch at ~ 7.15 THz at the zone center. The point of intersection is marked by a red circle in Fig. 3(a). This phonon mode displaces the atoms in a manner that reduces the Cr-Cr DMI along the c -axis and increases the Cr-Cr J_{zz} exchange interactions. The combined effect leads to a canting of the spins along the c -axis, shown in Fig. 3(c). This displacement minimally impacts the interlayer anisotropic exchange, and thus the magnetic structure retains the helical order in the ab -plane, but the canting of the spins along the c -axis leads to a conical chiral helimagnet (CCHM) phase, schematically shown in Fig. 1(f). The laser pulse efficiently excites the 7.15 THz phonon mode, which in turn leads to a phase transition between the two CHM and CCHM phases.

B. The spin dynamics under finite external magnetic fields

With our results on the laser-induced magnetism and observation of a phase transition to the chiral conical phase at zero magnetic fields, we proceed by investigating the spin dynamics under magnetic fields. At finite external magnetic fields, a nonzero net magnetic moment is generated by the

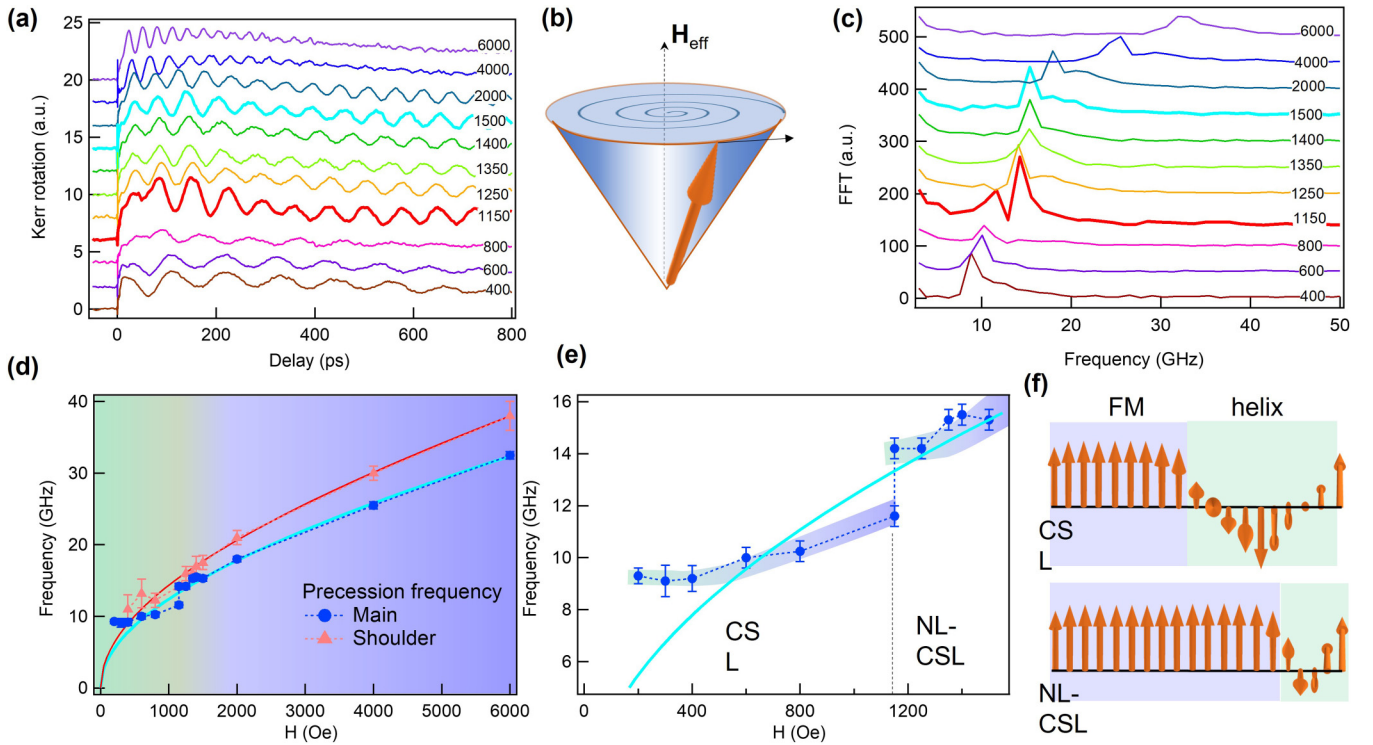


FIG. 4. Spin precession spanning over all phases at 6 K. (a) TR-MOKE signal at different magnetic fields. The numbers indicate the applied magnetic field in Oe. The data are offset for clarity. The thicker lines at 1150 and 1500 Oe mark phase-transition boundaries. (b) Schematic of the spin precession following the LLG motion. (c) Fourier transform of the data shown in (a). The red curve at 1150 Oe has two distinct frequencies. (d) Spin precession frequencies as a function of magnetic field obtained from (c). The blue area indicates the FFM phase. The error bars reflect the uncertainty from the Fourier transform. The solid curves are the fits using the Kittel equation for the FFM phase only. (e) Zoom-in plot of (d) at lower fields in the CSL phase showing a frequency onset at 9.1 GHz. There is an abrupt change of the frequency at the phase boundary between the L-CSL and the NL-CSL phases. (f) Spin textures for L-CSL and NL-CSL contain small and large ferromagnetic arrays, respectively.

fields. Figure 4(a) shows the Kerr rotation at 6 K across different phases, as the in-plane magnetic field is increased. Upon optical excitation, the magnetic moment is perturbed and deflected from its equilibrium direction, schematically shown in Fig. 4(b). The magnetization \mathbf{M} experiences a torque and precesses around the effective magnetic field \mathbf{H}_{eff} , following the Landau-Lifshitz-Gilbert (LLG) equation as given by [48]

$$\frac{\partial \mathbf{M}}{\partial t} = \gamma \mathbf{M} \times \mathbf{H}_{\text{eff}} - \frac{\alpha}{M} \left(\mathbf{M} \times \frac{\partial \mathbf{M}}{\partial t} \right), \quad (1)$$

where α is the phenomenological damping constant, $\gamma = 2.8 * \pi * g$ MHz/Oe is the gyromagnetic ratio of the electron, and g is the Landau splitting factor. The first term describes the magnetization precession, and the second term, also known as the Gilbert's term, leads to damping. At low temperature and at magnetic fields above 1500 Oe, the $\text{Cr}_{1/3}\text{NbS}_2$ crystal is in the FFM phase. In this magnetic phase, the magnetization precession persists longer at lower fields, whereas stronger damping is observed at higher fields, as can be observed in Fig. 4(a). At 1500 Oe the oscillations persist beyond 800 ps, whereas at 6000 Oe no oscillations can be observed beyond ~ 400 ps. This behavior could indicate stronger magnetic rigidity at higher magnetic fields. Upon switching the direction of the magnetic field, we observe a 180° phase change of the oscillations.

However, on decreasing the magnetic field from 1500 to 400 Oe, the crystal undergoes multiple magnetic phase transformations, from FFM, to a nonlinear chiral soliton lattice (NL-CSL), to a linear chiral soliton lattice (L-CSL), respectively. The Fourier transform of the spin precession data is shown in Fig. 4(c), and it yields a main frequency peak that spans from 9 to 30 GHz, accompanied by a higher-frequency shoulder with a lower amplitude. At the boundary between L-CSL and NL-CSL phases, which occurs at ~ 1150 Oe (red line), the Fourier transform shows two distinct frequency peaks making an abrupt change in the frequency. In the FFM phase, where the magnetization is more uniform, the precession frequency as a function of the in-plane magnetic field can be described by the Kittel equation [49,50]:

$$f = \frac{\gamma}{2\pi} \sqrt{H(H + 4\pi M_s)}, \quad (2)$$

where H is the magnetic field and M_s is magnetization. In Fig. 4(d), the precession frequency is plotted as a function of the magnetic field together with curves fit using Eq. (2) for the two observed frequencies. In the FFM phase, at magnetic fields higher than 1500 Oe, the experimental data can be well described by the Kittel equation. However, at lower magnetic fields between the L-CSL and NL-CSL phases, we observe a discontinuity of the precession frequency that deviates from the behavior described by the Kittel formula. In Fig. 4(e)

we plot the precession frequency of the main resonance as a function of the external magnetic field at lower fields. We not only observe a discontinuity at the phase boundary between the L-CSL and NL-CSL phases, but the precession frequency plateaus at around 9 GHz instead of decaying to zero. At lower magnetic field, the L-CSL phase contains part of the ferromagnetic phase mixed with helical spins, as shown in Fig. 4(f). As the magnetic field increases further to the NL-CSL phase, the ferromagnetic spin component increases further until the FFM phase dominates above 1500 Oe. The mixed spin texture of the L-CSL and NL-CSL phases is thought to be the underlying cause of the deviation of the precession frequency with magnetic fields from the prescribed Kittel formula [14,17,51,52]. To further investigate the role that spin-phonon interactions may play, we plot the spin precession frequencies as a function of the external magnetic field at various temperatures. At high temperatures (125 and 130 K), the spin precession can only be observed at magnetic fields above 1000 and 2000 Oe, respectively. As is the case for 6 K, the data exhibit a plateau at low fields with an onset that depends on the temperature. However, the plateau is less distinct and has a lower frequency value with increasing temperature, indicating that phonons are likely destroying the intrinsic spin ordering. Finally, the precession frequency in the FFM phase for three magnetic fields, 2000, 4000, and 6000 Oe, together with the magnetization saturation, is obtained through fitting, and it is in good agreement with the expected ferromagnetic resonance behavior, in which the precession frequency decreases with the increasing temperature (data available in the Supplemental Material [47]) [53].

III. CONCLUSIONS

In the absence of external magnetic fields, we have shown that an elastic distortion leading to spin canting in the chiral helimagnet $\text{Cr}_{1/3}\text{NbS}_2$ can be generated by an ultrafast laser pulse. The canting of the spin structure is due to the efficient spin-magnon coupling with specific phonon modes obtained theoretically. The canting of the spins leads to a slow phase transition from zero net magnetization to a nonzero magnetization. At finite external magnetic fields we also observed magnetization precession, which at higher magnetic fields in the FFM phase follows the Kittel formula of ferromagnetic resonance. However, at lower external magnetic fields, as the crystal enters the CSL phase, we observe clear deviations from the Kittel formula.

IV. MATERIALS AND METHODS

The single crystal of $\text{Cr}_{1/3}\text{NbS}_2$ was synthesized by a chemical vapor transport using iodine as the transport agent [54] with the H - T phase diagram under the perpendicular magnetic field to the c -axis as presented in Fig. 1. Magnetization versus temperature (M - T) and magnetic field (M - H) measurements were performed using a quantum design physical property measurement system (PPMS) with a vibrating sample magnetometer (VSM) option. The TR-MOKE was performed using a 1 kHz regenerative amplifier laser system (800 nm, 100 fs, Spectra Physics Inc.). A linearly polarized

laser beam at 800 nm was split into two parts; a small portion was sent to a delay stage for the probe, and the other portion was up-converted to 400 nm using a BBO crystal for use as a pump beam. The pump and probe beams were focused on the sample with diameters of 1 mm and 200 μm , respectively. The pump and probe powers were 2.5 mW and 90 μW , respectively. The pump fluence was kept low in the linear regime where the dynamics do not change with the pump fluence. A half-wave plate was used to rotate the polarization of the reflected beam. The probe beam was split to equal amounts of σ - and π -polarized beams by the Wollstone polarizer and detected by a balanced photodiode detector. The sample was kept inside a nonmagnetic variable temperature microstat (6–300 K), and the sample within the tail of the microstat was placed between the poles of an electromagnet. The magnetic field was measured at the sample using a Hall device.

We employed first-principles calculations within density functional theory [55,56] (DFT) as it is implemented in VASP [57,58] (version 5.4.4), using the projected augmented wave (PAW) method [59]. The exchange correlation functional was approximated with the PBEsol48 generalized gradient approximation (GGA) functional. The pseudopotentials included 11 electrons from Nb, 6 electrons from S, and 12 electrons from Cr with the electron configurations Nb : $4p^65s^14d^4$ (version Nb_{pv} 08Apr2002), S : $3s^23p^4$ (version S 06Sep2000), and Cr : $3p^63d^54s^1$ (version Cr_{pv} 02Aug2007). The plane-wave basis was expanded up to a cutoff of 500 eV, and the Brillouin zone was sampled on a $6 \times 6 \times 3$ Monkhorst-Pack mesh grid such that the total energy was converged to 1 meV/at. The atomic relaxation was performed using a $12 \times 12 \times 5$ Monkhorst-Pack mesh grid until the interatomic forces were no larger than 1 meV/Å. The phonons were calculated using the frozen core method within a $3 \times 3 \times 1$ supercell in conjunction with PHONOPY [60]. For the phonons, the van der Waals interaction was included using the DFT-D3 [61] Grimme method with Becke-Jonson damping [62]. The magnetic exchange coupling parameters were calculated from the Heisenberg Hamiltonian, written as

$$E = - \sum_i K_i \mathbf{S}_i \cdot \mathbf{S}_i - \sum_{ij, i \neq j} [J_{ij}^{\text{iso}} \mathbf{S}_i \cdot \mathbf{S}_j + \mathbf{S}_i J_{ij}^{\text{ani}} \mathbf{S}_j + \mathbf{D}_{ij} \cdot (\mathbf{S}_i \times \mathbf{S}_j)]. \quad (3)$$

Here, K_i is the single-ion anisotropy, J_{ij} is the symmetric exchange, D_{ij} is the DMI vector, and \mathbf{S}_i is the spin, which is normalized to 1. The exchange parameters were calculated using the TB2J [63] python package, which calculates the exchange integrals directly from a projected tight-binding Hamiltonian [64,65]. We used WANNIER90 [66] to create the tight-binding model in which the Kohn-Sham orbitals were projected over Wannier functions for the Cr d -orbitals, Nb d -orbitals, and S p -orbitals. The initial projections were considered to be maximally localized when the difference of the spread functional between iterations was less than 10^{-10} \AA^2 . The Monte Carlo simulations were performed as implemented *ab initio* [67,68], using the output files generated by TB2J [69].

ACKNOWLEDGMENTS

This work was in part supported by the National Science Foundation under Grant No. ECCS-1952957. M.-H.P. and H.S. acknowledge support from the U.S. Department

of Energy, Office of Basic Energy Sciences, Division of Materials Sciences and Engineering under Award No. DE-FG02-07ER46438. D.M. acknowledges support from the Gordon and Betty Moore Foundation's EPIQS Initiative, Grant GBMF9069.

- [1] T. Moriya, Anisotropic superexchange interaction and weak ferromagnetism, *Phys. Rev.* **120**, 91 (1960).
- [2] I. Dzyaloshinsky, A thermodynamic theory of 'weak' ferromagnetism of antiferromagnetics, *J. Phys. Chem. Solids* **4**, 241 (1958).
- [3] S. V. Maleyev, Cubic magnets with Dzyaloshinskii-Moriya interaction at low temperature, *Phys. Rev. B* **73**, 174402 (2006).
- [4] T. Moriya and T. Miyadai, Evidence for the helical spin structure due to antisymmetric exchange interaction in $\text{Cr}_{1/3}\text{NbS}_2$, *Solid State Commun.* **42**, 209 (1982).
- [5] S. Mühlbauer, B. Binz, F. Jonietz, C. Pfleiderer, A. Rosch, A. Neubauer, R. Georgii, and P. Böni, Skyrmion lattice in a chiral magnet, *Science* **323**, 915 (2009).
- [6] S. Zhang, G. van der Laan, J. Müller, L. Heinen, M. Garst, A. Bauer, H. Berger, C. Pfleiderer, and T. Hesjedal, Reciprocal space tomography of 3D skyrmion lattice order in a chiral magnet, *Proc. Natl. Acad. Sci. (USA)* **115**, 6386 (2018).
- [7] S. L. Zhang, I. Stasinopoulos, T. Lancaster, F. Xiao, A. Bauer, F. Rucker, A. A. Baker, A. I. Figueroa, Z. Salman, F. L. Pratt, S. J. Blundell, T. Prokscha, A. Suter, J. Waizner, M. Garst, D. Grundler, G. van der Laan, C. Pfleiderer, and T. Hesjedal, Room-temperature helimagnetism in FeGe thin films, *Sci. Rep.* **7**, 123 (2017).
- [8] M. N. Wilson, E. A. Karhu, D. P. Lake, A. S. Quigley, S. Meynell, A. N. Bogdanov, H. Fritzsche, U. K. Röbber, and T. L. Monchesky, Discrete helicoidal states in chiral magnetic thin films, *Phys. Rev. B* **88**, 214420 (2013).
- [9] N. Jiang, Y. Nii, H. Arisawa, E. Saitoh, and Y. Onose, Electric current control of spin helicity in an itinerant helimagnet, *Nat. Commun.* **11**, 1601 (2020).
- [10] S. Seki, X. Z. Yu, S. Ishiwata, and Y. Tokura, Observation of skyrmions in a multiferroic material, *Science* **336**, 198 (2012).
- [11] Y. Togawa, T. Koyama, K. Takayanagi, S. Mori, Y. Kousaka, J. Akimitsu, S. Nishihara, K. Inoue, A. S. Ovchinnikov, and J. Kishine, Chiral Magnetic Soliton Lattice on a Chiral Helimagnet, *Phys. Rev. Lett.* **108**, 107202 (2012).
- [12] N. Sirica, P. Vilmercati, F. Bondino, I. Pis, S. Nappini, S. K. Mo, A. V. Fedorov, P. K. Das, I. Vobornik, J. Fujii, L. Li, D. Sapkota, D. S. Parker, D. G. Mandrus, and N. Mannella, The nature of ferromagnetism in the chiral helimagnet $\text{Cr}_{1/3}\text{NbS}_2$, *Commun. Phys.* **3**, 65 (2020).
- [13] Y. Cao, Z. Huang, Yin, H. Xie, Liu, W. Wang, C. Zhu, D. Mandrus, L. Wang, and W. Huang, Overview and advances in a layered chiral helimagnet $\text{Cr}_{1/3}\text{NbS}_2$, *Mater. Today Adv.* **7**, 100080 (2020).
- [14] J. I. Yonemura, Y. Shimamoto, T. Kida, D. Yoshizawa, Y. Kousaka, S. Nishihara, F. J. T. Goncalves, J. Akimitsu, K. Inoue, M. Hagiwara, and Y. Togawa, Magnetic solitons and magnetic phase diagram of the hexagonal chiral crystal CrNb_3S_6 in oblique magnetic fields, *Phys. Rev. B* **96**, 184423 (2017).
- [15] A. C. Bornstein, B. J. Chapman, N. J. Ghimire, D. G. Mandrus, D. S. Parker, and M. Lee, Out-of-plane spin-orientation dependent magnetotransport properties in the anisotropic helimagnet $\text{Cr}_{1/3}\text{NbS}_2$, *Phys. Rev. B* **91**, 184401 (2015).
- [16] R. Khoshlahni, A. Qaiumzadeh, A. Bergman, and A. Brataas, Ultrafast generation and dynamics of isolated skyrmions in antiferromagnetic insulators, *Phys. Rev. B* **99**, 054423 (2019).
- [17] K. Hoshi, J.-I. Kishine, and J.-I. Ohe, Coupled-oscillator collective mode of a magnetic chiral soliton lattice, *Phys. Rev. B* **102**, 134414 (2020).
- [18] Y. Togawa, T. Koyama, Y. Nishimori, Y. Matsumoto, S. McVitie, D. McGrouther, R. L. Stamps, Y. Kousaka, J. Akimitsu, S. Nishihara, K. Inoue, I. G. Bostrem, V. E. Sinityn, A. S. Ovchinnikov, and J. Kishine, Magnetic soliton confinement and discretization effects arising from macroscopic coherence in a chiral spin soliton lattice, *Phys. Rev. B* **92**, 220412(R) (2015).
- [19] A. V. Kimel and M. Li, Writing magnetic memory with ultrashort light pulses, *Nat. Rev. Mater.* **4**, 189 (2019).
- [20] K. Tsuruta, M. Mito, H. Deguchi, J. Kishine, Y. Kousaka, J. Akimitsu, and K. Inoue, Phase diagram of the chiral magnet $\text{Cr}_{1/3}\text{NbS}_2$ in a magnetic field, *Phys. Rev. B* **93**, 104402 (2016).
- [21] E. M. Clements, R. Das, M.-H. Phan, L. Li, V. Keppens, D. Mandrus, M. Osofsky, and H. Srikanth, Magnetic field dependence of nonlinear magnetic response and tricritical point in the monoaxial chiral helimagnet $\text{Cr}_{1/3}\text{NbS}_2$, *Phys. Rev. B* **97**, 214438 (2018).
- [22] N. Sirica, H. Hedayat, D. Bugini, M. R. Koehler, L. Li, D. S. Parker, D. G. Mandrus, C. Dallera, E. Carpena, and N. Mannella, Disentangling electronic, lattice, and spin dynamics in the chiral helimagnet $\text{Cr}_{1/3}\text{NbS}_2$, *Phys. Rev. B* **104**, 174426 (2021).
- [23] E. M. Clements, R. Das, L. Li, P. J. Lampen-Kelley, M.-H. Phan, V. Keppens, D. Mandrus, and H. Srikanth, Critical behavior and macroscopic phase diagram of the monoaxial chiral helimagnet $\text{Cr}_{1/3}\text{NbS}_2$, *Sci. Rep.* **7**, 6545 (2017).
- [24] E. Beaurepaire, J. C. Merle, A. Daunois, and J. Y. Bigot, Ultrafast Spin Dynamics in Ferromagnetic Nickel, *Phys. Rev. Lett.* **76**, 4250 (1996).
- [25] B. Koopmans, M. van Kampen, J. T. Kohlhepp, and W. J. M. de Jonge, Ultrafast Magneto-Optics in Nickel: Magnetism or Optics? *Phys. Rev. Lett.* **85**, 844 (2000).
- [26] A. V. Kimel, R. V. Pisarev, J. Hohlfeld, and Th. Rasing, Ultrafast Quenching of the Antiferromagnetic Order in FeBO_3 : Direct Optical Probing of the Phonon-Magnon Coupling, *Phys. Rev. Lett.* **89**, 287401 (2002).
- [27] B. Koopmans, G. Malinowski, F. Dalla Longa, D. Steiauf, M. Fähnle, T. Roth, M. Cinchetti, and M. Aeschlimann, Explaining the paradoxical diversity of ultrafast laser-induced demagnetization, *Nat. Mat.* **9**, 259 (2009).
- [28] L. Guidoni, E. Beaurepaire, and J. Y. Bigot, Magneto-Optics

- in the Ultrafast Regime: Thermalization of Spin Populations in Ferromagnetic Films, *Phys. Rev. Lett.* **89**, 017401 (2002).
- [29] J. Y. Bigot, M. Vomir, and E. Beaurepaire, Coherent ultrafast magnetism induced by femtosecond laser pulses, *Nat. Phys.* **5**, 515 (2009).
- [30] A. V. Kimel, A. Kirilyuk, A. Tsvetkov, R. V. Pisarev, and Th. Rasing, Laser-induced ultrafast spin reorientation in the antiferromagnet TmFeO₃, *Nature (London)* **429**, 850 (2004).
- [31] A. Kimel, A. Kirilyuk, P. Usachev, R. Pisarev, A. Balbashov, and T. Rasing, Ultrafast non-thermal control of magnetization by instantaneous photomagnetic pulses, *Nature (London)* **435**, 655 (2005).
- [32] G. M. Choi, A. Schleife, and D. G. Cahill, Optical-helicity-driven magnetization dynamics in metallic ferromagnets, *Nat. Commun.* **8**, 15085 (2017).
- [33] O. H.-C. Cheng, D. H. Son, and M. Sheldon, Light-induced magnetism in plasmonic gold nanoparticles, *Nat. Photon.* **14**, 365 (2020).
- [34] A. Stupakiewicz, K. Szerenos, D. Afanasiev, A. Kirilyuk, and A. V. Kimel, Ultrafast nonthermal photo-magnetic recording in a transparent medium, *Nature (London)* **542**, 71 (2017).
- [35] C. Tzschaschel, K. Otani, R. Iida, T. Shimura, H. Ueda, S. Günther, M. Fiebig, and T. Satoh, Ultrafast optical excitation of coherent magnons in antiferromagnetic NiO, *Phys. Rev. B* **95**, 174407 (2017).
- [36] A. A. Fisher, E. F. C. Dreyer, A. Chakrabarty, and S. C. Rand, Optical magnetization, Part II: Theory of induced optical magnetism, *Opt. Express* **24**, 26064 (2016).
- [37] M. T. Trinh, K. Makhali, E. Dreyer, A. Shanker, S. J. Yoon, J. Kim, and S. Rand, Optical torque induces magnetism at the molecular level, *Opt. Express* **27**, 21295 (2019).
- [38] A. M. Kalashnikova, A. V. Kimel, R. V. Pisarev, V. N. Gridnev, A. Kirilyuk, and T. Rasing, Impulsive Generation of Coherent Magnons by Linearly Polarized Light in the Easy-Plane Antiferromagnet FeBO₃, *Phys. Rev. Lett.* **99**, 167205 (2007).
- [39] A. Kimel, B. Ivanov, R. Pisarev, P. Usachev, A. Kirilyuk, and T. Rasing, Inertia-driven spin switching in antiferromagnets, *Nat. Phys.* **5**, 727 (2009).
- [40] G. Ju, J. Hohlfeld, B. Bergman, R. J. M. van de Veerdonk, O. N. Mryasov, J.-Y. Kim, X. Wu, D. Weller, and B. Koopmans, Ultrafast Generation of Ferromagnetic Order via a Laser-Induced Phase Transformation in Ferri-Thin Films, *Phys. Rev. Lett.* **93**, 197403 (2004).
- [41] J.-U. Thiele, M. Buess, and C. H. Back, Spin dynamics of the antiferromagnetic-to-ferromagnetic phase transition in ferri on a sub-picosecond time scale, *Appl. Phys. Lett.* **85**, 2857 (2004).
- [42] B. Bergman, G. Ju, J. Hohlfeld, R. J. M. van de Veerdonk, J.-Y. Kim, X. Wu, D. Weller, and B. Koopmans, Identifying growth mechanisms for laser-induced magnetization in ferri, *Phys. Rev. B* **73**, 060407(R) (2006).
- [43] I. Radu, C. Stamm, N. Pontius, T. Kachel, P. Ramm, J.-U. Thiele, H. A. Dürr, and C. H. Back, Laser-induced generation and quenching of magnetization on ferri studied with time-resolved x-ray magnetic circular dichroism, *Phys. Rev. B* **81**, 104415 (2010).
- [44] S. O. Mariager, F. Pressacco, G. Ingold, A. Caviezel, E. Möhr-Vorobeva, P. Beaud, S. L. Johnson, C. J. Milne, E. Mancini, S. Moyerman, E. E. Fullerton, R. Feidenhans'l, C. H. Back, and C. Quitmann, Structural and Magnetic Dynamics of a Laser Induced Phase Transition in Ferri, *Phys. Rev. Lett.* **108**, 087201 (2012).
- [45] F. Quirin, M. Vattilana, U. Shymanovich, A.-E. El-Kamhawy, A. Tarasevitch, J. Hohlfeld, D. von der Linde, and K. Sokolowski-Tinten, Structural dynamics in ferri during a laser-induced metamagnetic phase transition, *Phys. Rev. B* **85**, 020103(R) (2012).
- [46] F. Pressacco, D. Sangalli, V. Uhlíř, D. Kutnyakhov, J. Ander Arregi, S. Ymir Agustsson, G. Brenner, H. Redlin, M. Heber, D. Vasilyev, J. Demsar, G. Schönhense, M. Gatti, W. Marini, A. Würth, and F. Sirotti, Subpicosecond metamagnetic phase transition in ferri driven by non-equilibrium electron dynamics, *Nat. Commun.* **12**, 5088 (2021).
- [47] See Supplemental Material at <http://link.aps.org/supplemental/10.1103/PhysRevB.106.035103> for a description of the theoretical formalism used in the calculations and supporting experimental data.
- [48] T. L. Gilbert, A phenomenological theory of damping in ferromagnetic materials, *IEEE Trans. Magn.* **40**, 3443 (2004).
- [49] Y. Wei, R. Brucas, K. Gunnarsson, I. Harward, Z. Celinski, and P. Svedlindh, Static and dynamic magnetic properties of bcc Fe₄₉Co₄₉V₂ thin films on Si(1 0 0) substrates, *J. Phys. D* **46**, 495002 (2013).
- [50] C. Kittel, On the theory of ferromagnetic resonance absorption, *Phys. Rev.* **73**, 155 (1948).
- [51] J. I. Kishine and A. S. Ovchinnikov, Theory of monoaxial chiral helimagnet, *Solid State Phys.* **66**, 1 (2015).
- [52] Y. Shimamoto, F. J. T. Goncalves, T. Sogo, Y. Kousaka, and Y. Togawa, Switching behavior of the magnetic resonance in a monoaxial chiral magnetic crystal CrNb₃S₆, *Appl. Phys. Lett.* **115**, 242401 (2019).
- [53] W. Jantz, W. Wuttling, and J. R. Sandercock, Determination of magnetic and elastic properties of FeBO₃ by light scattering, *J. Phys. C* **9**, 2229 (1976).
- [54] N. J. Ghimire, M. A. McGuire, D. S. Parker, B. Sipos, S. Tang, J. Q. Yan, B. C. Sales, and D. Mandrus, Magnetic phase transition in single crystals of the chiral helimagnet Cr_{1/3}NbS₂, *Phys. Rev. B* **87**, 104403 (2013).
- [55] W. Kohn and L. J. Sham, Self-consistent equations including exchange and correlation effects, *Phys. Rev.* **140**, A1133 (1965).
- [56] P. Hohenberg and W. Kohn, Inhomogeneous electron gas, *Phys. Rev.* **136**, B864 (1964).
- [57] G. Kresse and J. Furthmüller, Efficient iterative schemes for *ab initio* total-energy calculations using a plane-wave basis set, *Phys. Rev. B* **54**, 11169 (1996).
- [58] G. Kresse and D. Joubert, From ultrasoft pseudopotentials to the projector augmented-wave method, *Phys. Rev. B* **59**, 1758 (1999).
- [59] P. E. Blöchl, Projector augmented-wave method, *Phys. Rev. B* **50**, 17953 (1994).
- [60] A. Togo and I. Tanaka, First principles phonon calculations in materials science, *Scr. Mater.* **108**, 1 (2015).
- [61] S. Grimme, J. Antony, S. Ehrlich, and H. Krieg, A consistent and accurate *ab initio* parametrization of density functional dispersion correction (DFT-D) for the 94 elements H-Pu, *J. Chem. Phys.* **132**, 154104 (2010).
- [62] S. Grimme, S. Ehrlich, and L. Goerigk, Effect of the damping function in dispersion corrected density functional theory, *J. Comput. Chem.* **32**, 1456 (2011).

- [63] X. He, N. Helbig, M. J. Verstraete, and E. Bousquet, TB2J: A python package for computing magnetic interaction parameters, *Comput. Phys. Commun.* **264**, 107938 (2021).
- [64] A. I. Liechtenstein, M. I. Katsnelson, V. P. Antropov, and V. A. Gubanov, Local spin density functional approach to the theory of exchange interactions in ferromagnetic metals and alloys, *J. Magn. Magn. Mater.* **67**, 65 (1987).
- [65] D. M. Korotin, V. V. Mazurenko, V. I. Anisimov, and S. V. Streltsov, Calculation of exchange constants of the Heisenberg model in plane-wave-based methods using the Green's function approach, *Phys. Rev. B* **91**, 224405 (2015).
- [66] G. Pizzi, V. Vitale, R. Arita, S. Blügel, F. Freimuth, G. Géranton, M. Gibertini, D. Gresch, C. Johnson, T. Koretsune, J. Ibañez-Azpiroz, H. Lee, J. M. Lihm, D. Marchand, A. Marrazzo, Y. Mokrousov, J. I. Mustafa, Y. Nohara, Y. Nomura, L. Paulatto *et al.*, Wannier90 as a community code: New features and applications, *J. Phys.: Condens. Matter* **32**, 165902 (2020).
- [67] X. Gonze, B. Amadon, G. Antonius, F. Arnardi, L. Baguet, J.-M. Beuken, J. Bieder, F. Bottin, J. Bouchet, E. Bousquet, N. Brouwer, F. Bruneval, G. Brunin, T. Cavignac, J.-B. Charraud, W. Chen, M. Côté, S. Cottenier, J. Denier, and J. Zwanziger, The Abinitproject: Impact, environment and recent developments, *Comput. Phys. Commun.* **248**, 107042 (2020).
- [68] A. H. Romero, D. Allan, B. Amadon, G. Antonius, T. Applencourt, L. Baguet, J. Bieder, F. Bottin, J. Bouchet, E. Bousquet, F. Bruneval, G. Brunin, D. Caliste, M. Côté, J. Denier, C. Dreyer, P. Ghosez, M. Giantomassi, Y. Gillet, and X. Gonze, ABINIT: Overview and focus on selected capabilities, *J. Chem. Phys.* **152**, 124102 (2020).
- [69] J. P. Perdew, A. Ruzsinszky, G. I. Csonka, O. A. Vydrov, G. E. Scuseria, L. A. Constantin, X. Zhou, and K. Burke, Restoring the Density-Gradient Expansion for Exchange in Solids and Surfaces, *Phys. Rev. Lett.* **100**, 136406 (2008).